Exp Fluids (2010) 49:701–712
DOI 10.1007/s00348-010-0837-9

RESEARCH ARTICLE

Improvement of measurement accuracy in micro PIV by image overlapping

Chuong Vinh Nguyen · Andreas Fouras · Josie Carberry

Received: 9 June 2009 / Revised: 27 January 2010 / Accepted: 28 January 2010 / Published online: 4 March 2010

Abstract Micro PIV uses volume illumination; therefore, the velocity measured at the focal plane is a weighted average of the velocities within the measurement volume. The contribution of out-of-focus particles to the PIV correlation can generate significant measurement errors particularly in near wall regions. We present a new application of image overlapping, which is shown to be very effective in improving the accuracy of time-averaged velocity measurements by effectively reducing the measurement depth. The performance of image overlapping and correlation averaging were studied using synthetic and experimental images of micro channel flow, both with and without image pre-processing. The results show that for flows without particle clumping, image overlapping provides the best measurement accuracy without any need for image pre-processing. For flows with particle clumping, image overlapping combined with band-pass filtering provides the best measurement accuracy. When overlapped images are saturated with particles due to a large number of image pairs, image overlapping measurement still does not show any visible pixel-locking effect. Image overlapping was found to have comparable or slightly reduced pixel-locking effects compared to correlation averaging. In addition, image overlapping utilizes significantly fewer computational resources than the other techniques.

C. V. Nguyen · A. Fouras · J. Carberry
Fluid Laboratory for Aeronautical and Industrial Research (FLAIR), Monash University, Melbourne, VIC 3800, Australia
e-mail: chuong.nguyen@eng.monash.edu.au

A. Fouras (✉)
Division of Biological Engineering, Monash University, Melbourne, VIC 3800, Australia
e-mail: fouras@eng.monash.edu

Nomenclature

δx, δy	Horizontal and vertical displacements in pixels
δz_{corr}	Depth of correlation
λ	Fluorescent wavelength
$\Phi_k(\delta x, \delta y)$	Correlation function from an image pair
$\Phi_{\text{ens}}(\delta x, \delta y)$	Averaged correlation function
$\Phi_{\text{ovl}}(\delta x, \delta y)$	Correlation function from an overlapped image pairs
NA	Numerical aperture
ε	Signal threshold where depth of correlation ends
d_p	Particle diameter
$I_k(i, j)$, $I'_k(i, j)$	First and second image exposures
M	Lens magnification
N_p	Number of particles per image
P, Q	Image width and height
R	Half of channel height
U^*	Normalized velocity
U_c^*	Normalized velocity at the center, $z = 0$
U_w^*	Normalized velocity near the wall, $z = 0.9R$

1 Introduction

PIV was introduced over two decades ago to measure velocity components in a planar region illuminated by a thin laser sheet (Adrian [2]). To measure micro flow fields, an extension of PIV named micro PIV was developed (Santiago et al. [21]). A typical micro PIV system utilizes an epi-fluorescent microscope, fluorescent seed particles and an intensified camera. Due to the small scale, only volume illumination is currently feasible. Thus in micro

PIV, the depth over which the measurement is taken is the distance over which the particles, both in-focus and out-of-focus, significantly affect the measurement. The depth of measurement is characterized by "the depth of correlation" of the imaging system (Wereley et al. [23], Olsen and Adrian [16], Bourdon et al. [6]), where the depth of correlation is defined as the depth over which the correlation signal of particles significantly contribute to the correlation function. A threshold ε is chosen below which the particle's correlation signal is considered negligible. Typically, ε is 1% of the maximum correlation provided by the in-focus particles (Olsen and Adrian [16]). The change of the particle images and their correlation signals with respect to the depth, or z-direction, is illustrated in Fig. 1. In the basic form, the depth of correlation can be calculated according to Olsen and Adrian [16]:

$$\delta z_{\text{corr}} = 2\left[\frac{1-\sqrt{\varepsilon}}{\sqrt{\varepsilon}}\left(\frac{d_p^2}{4NA^2}+\frac{5.95(M+1)^2\lambda^2}{16M^4NA^4}\right)\right]^{\frac{1}{2}} \quad (1)$$

Bourdon et al. [5] defined the depth of correlation based on the curvature of the correlation function and obtained the same result. The depth of correlation can be increased by Brownian motion (Olsen and Adrian [17]), out-of-plane motion (Olsen and Bourdon [18]) and in-plane shear (Olsen [19]).

As demonstrated in Fig. 1, the velocity measurement is a weighted average of the velocities within the measurement volume. In regions where the contributions of the

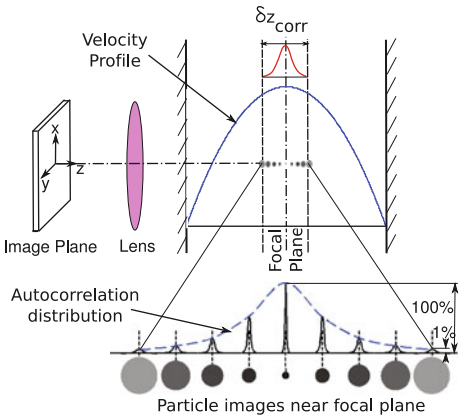

Fig. 1 Schematic showing the optical setup for micro PIV of channel flow. The velocity profile is shown as a *parabolic curve*. The focal plane is located at the center of the channel. Particles further from the focal plane appear larger and dimmer and the strength of the corresponding peak of auto-correlation decreases. The depth of correlation, δz_{corr}, is defined as the distance over which the ratio of the auto-correlation to the auto-correlation at the focal plane is greater than ε (chosen to be 1% in Olsen and Adrian [16]). Due to the variation of particle correlation signal over δz_{corr}, the measured velocity is a weighted sum of the velocities within the depth of correlation

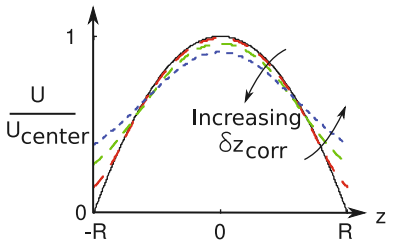

Fig. 2 Effect of increasing the depth of correlation, δz_{corr}, on the measurement of a parabolic normalized velocity profile. The *solid line* is the true profile, and the *dashed lines* are the velocity profiles measured with a finite δz_{corr}. The *arrows* indicate the effect of increasing δz_{corr}. With increasing depth of correlation, the measured velocity in the center of the channel is smaller than the exact velocity, while the velocity at the wall is greater than the exact value of zero

out-of-focus particles either side of the focal plane are not equal and opposite a bias error results. This effect may be exacerbated by non-uniform seeding densities, particularly for near wall measurements. Fig. 2 shows the effect of depth of correlation on the measurement of a parabolic velocity profile, where higher δz_{corr} values result in larger errors. For higher δz_{corr}, the velocity is underestimated in the flow center and overestimated at the wall, but as δz_{corr} decreases the measurement values converge toward the true value.

In many cases, significant depth of correlation and the associated errors are unavoidable due to low numerical aperture imaging systems and other factors that increase the depth of correlation as mentioned earlier: Brownian motion, out-of-plane motion and in-plane shear. The problem is most severe for near wall flows, including biological shear flows (Nesbitt et al. [15]) where the velocity magnitude is small and the error is large. As a result, techniques for reducing depth of correlation and associated errors will be of utility to experimental practitioners.

1.1 Existing techniques to improve micro PIV measurements

The quality of time-invariant data can generally be improved by averaging. Time-averaged velocity fields can be obtained by vector averaging, whereby velocity vectors are averaged at each location. In PIV, as velocity vectors are obtained from correlation maps, time-averaged velocity can be also obtained from the averaged correlation maps. Correlation averaging or "ensemble correlation", proposed by Meinhart et al. [13] and Wereley et al. [22], is currently the first choice to analyze time-invariant micro PIV data. Although correlation averaging improves accuracy by improving the signal to noise ratio of the correlation peaks, the accuracy of the correlation peaks used in correlation averaging is still affected by the out-of-focus particles within the depth of correlation.

A number of techniques have been developed to improve the accuracy of micro PIV by reducing the effect of out-of-focus particles. Gui et al. [9] proposed a band-pass filtering technique called "micro PIV image filtering" to reduce both single pixel random noise and low-frequency background noise. This filtering technique removes background noise due to out-of-focus particles in a similar way to the phase-separation technique proposed by Kiger and Pan [10], except that Kiger and Pan used a median filter while Gui et al. used a mean filter. These techniques rely on the difference in the spatial frequency between in-focus particles, out-of-focus particles and noise. By adjusting the filter sizes, band-pass filtering can selectively pass the in-focus particles while suppressing the noise and the out-of-focus particles. The band-pass filtering proposed by Gui et al. [9] consists of two mean spatial filters, one with small filter size to remove high-spatial frequency noise and one with large filter size to remove low-spatial frequency noise. Lindken et al. [12] applied spatial filtering using a Gaussian filter, to improve the measurement accuracy in stereo micro PIV. In this paper, we utilize a band-pass median filter, a combination of Gui et al. [9] and Kiger and Pan [10], to reduce strong noise:

$$I_{\text{filt}}(i,j) = \text{median}(I(i,j),3) - \text{median}(I(i,j),2r_{\text{filt}}+1) \tag{2}$$

where median $(I(i, j), s)$ is a function returning the median value of a square $s \times s$ region centered around (i, j), and r_{filt} is the filter radius.

Our tests have confirmed that image pre-processing using Eq. 2 removes both background noise and out-of-focus particles. To reduce computational time, we utilize a constant-time median filtering algorithm developed by Perreult and Herbert [20].

To control the focal depth, i.e. depth of measurement, Bitsch et al. [3] proposed an image thresholding technique called "base-clipping". This technique relies on the fact that the intensity of the out-of-focus particles is lower than that of the in-focus particles. Therefore, a suitable threshold can separate and remove the out-focus particles. The image thresholding is performed as:

$$I_{\text{thres}}(i,j) = \begin{cases} 0 & \text{if } I(i,j) \le \text{threshold;} \\ I(i,j) - \text{threshold} & \text{if } I(i,j) > \text{threshold.} \end{cases} \tag{3}$$

A combination of image thresholding and band-pass filtering was employed by Zheng and Silvber-Li [25] in their velocity profile measurement of a micro channel. As an alternative to all of the earlier techniques, the depth of correlation can also be increased or decreased up to 2 times by power filtering (Bourdon et al. [4]).

Image thresholding and band-pass filtering are usually combined with correlation averaging. The combination can be done in 3 steps. First each image in an image set is pre-processed by band-pass filtering or image thresholding. Second, a cross-correlation function is applied to each image pair $I_k(i, j)$ & $I'_k(i, j)$ in the pre-processed image set:

$$\Phi_k(\delta x,\delta y) = \sum_{j=1}^{Q}\sum_{i=1}^{P} I_k(i+\delta x, j+\delta y) I'_k(i,j) \tag{4}$$

where P and Q are the image width and height.

Finally, the correlation maps obtained from a set of image pairs are averaged to produce a single correlation map, which is used to calculate the velocity:

$$\Phi_{\text{ens}}(\delta x,\delta y) = \frac{1}{N_{\text{pairs}}}\sum_{k=1}^{N_{\text{pairs}}} \Phi_k(\delta x,\delta y) \tag{5}$$

1.2 New application of image overlapping to reduce the effect of out-of-focus particles

The image overlapping technique was originally proposed by Wereley et al. [22] to increase the seeding density in recorded micro PIV images of steady flows. In our study, however, the application of image overlapping to micro PIV data was found to additionally reduce the effect of out-of-focus particles. Unlike the image averaging technique (Meinhart et al. [13]), which works by adding images together, image overlapping works by taking the maximum pixel intensity at each pixel location:

$$I_{\max}(i,j) = \max\left(I_k(i,j), k = 1,2,3,\ldots,N_{\text{pairs}}\right) \tag{6}$$

Thus, image overlapping can be considered as a maximum filtering technique which, when applied to a set of images, produces a single maximum or overlapped image. As shown in Fig. 1, particle intensity varies across the focal plane. The brightest particles are in-focus, close to the microscope focal plane. Further from the focal plane, the out-of-focus particles are dimmer. By collecting maximum pixel intensities, image overlapping collects the brightest particles while excluding dimmer particles at the same pixel locations. In this way, image overlapping collects the particles closest to the focal plane, effectively reducing the depth of measurement. For a set of double-exposure PIV images containing N_{pairs} image pairs, image overlapping produces a single image pair as shown in Fig. 3a. Cross-correlation is then applied to this overlapped image pair to obtain a time-averaged velocity field:

$$\Phi_{\text{ovl}}(\delta x,\delta y) = \sum_{j=1}^{Q}\sum_{i=1}^{P} I_{\max}(i+\delta x, j+\delta y) I'_{\max}(i,j) \tag{7}$$

Figure 4 shows the effect of using a different number of images, N_{pairs}, to produce the overlapped image. With

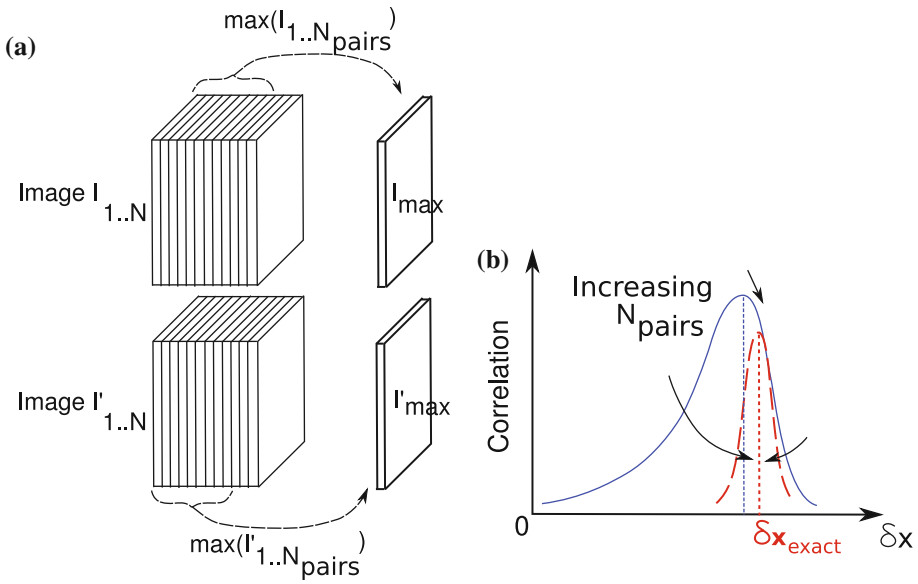

Fig. 3 Schematic showing the procedure to produce a pair of overlapped images I_{max} & I'_{max} from a set of N_{pairs} pairs and the effect of increasing N_{pairs} on the correlation peak at the center of a parabolic velocity profile. **a** Image series of the first and second exposures $I_{1..N\_pairs}$ & $I'_{1..N\_pairs}$ are overlapped by selecting the value of the maximum intensity at each pixel to produce a single image pair I_{max} & I'_{max}. **b** Correlation peak obtained from the image pair without and with image overlapping. Without image overlapping, due to the contribution from the out-of-focus particles traveling at a slower velocity, the center of the correlation peak (*solid curve*) is shifted toward zero, and the shape of the correlation peak is also skewed in this direction. Image overlapping reduces the contributions of particles further away from the focal plane. With increasing N_{pairs}, the peak (*dashed curve*) becomes narrower and its center moves toward the location of the exact displacement δx_{exact}

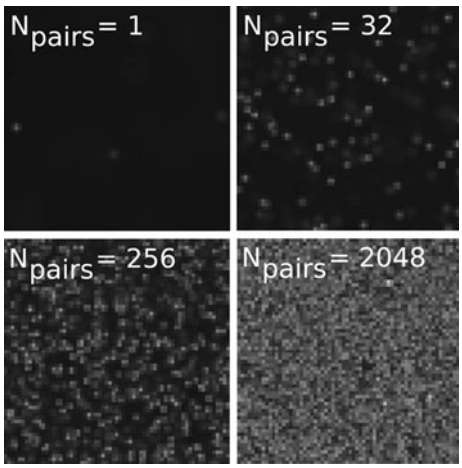

Fig. 4 Image templates produced by image overlapping with N_{pairs} = 1, 32, 256 and 2,048. Image size for each case is 64 × 64 pixels. For N_{pairs} = 1, there is an out-of-focus particle near the right edge of the image template. However, for $N_{pairs} \geq 256$, this particle is almost hidden behind other particles

increasing N_{pairs} more out-of-focus particles are discarded in favor of in-focus particles, and the resulting overlapped image contains mainly in-focus particles and yields more accurate velocity measurements.

When PIV is performed on images containing out-of-focus particles, the shape and location of the PIV correlation peaks contain contributions from both in-focus and out-of-focus particles. In the majority of cases, the contribution from the out-of-focus particles is unwanted as they may distort both the location and shape of the correlation peak. For example, the correlation peak with a measurement plane at the center of a parabolic velocity flow, typical of channel flow, will contain contributions from the out-of-focus particles traveling at a slower velocity. As shown by the solid curve in Fig. 3b, the center of the correlation peak will be shifted toward zero and the shape of the correlation peak will also be skewed in this direction. An ideal correlation peak contains only contributions from particles at the focal plane. When PIV is performed on an overlapped image pair, as shown in Fig. 3b, the peak of the correlation map becomes narrower (dashed curve) and its center moves toward the location of the exact velocity.

Like correlation averaging, image overlapping is only applicable to laminar and steady flow conditions within the acquisition time of overlapped images. Trying to apply image overlapping techniques to unsteady or turbulent flows can result in the broadening of correlation peaks of overlapped images due to the flow statistics (Adrian [1]). Further studies may be required to provide more insight of such broadening effect to the measurement accuracy of image overlapping. In the case of Brownian motion, significant Brownian motion can also broaden the correlation

peaks but cause no bias to the measurement accuracy (Olsen and Adrian [17]).

Image overlapping can also be combined with a pre-processing techniques such as band-pass filtering to further improve the measurement accuracy. This can be done in three steps. First, the pre-processing technique is applied to a set of double-exposure images. Then, the pre-processed image set is overlapped to produce a single image pair. Finally, the cross-correlation is applied to the overlapped image pair, and the correlation peak is fitted to produce velocity vectors.

An additional virtue of image overlapping is that it requires much less computational time than correlation averaging. In PIV, image correlation requires $O[N^2]$ operations if using direct correlation (as in Eq. 4) or $O[N\log_2 N]$ operations if using FFT-based correlation, performed on image region of N pixels. Correlation averaging performed on N_{pairs} image pairs includes N_{pairs} correlation calculations and $N_{\text{pairs}} - 1$ summations of correlation maps. Image overlapping performed on the same image set includes one correlation calculation and $2(N_{\text{pairs}} - 1)$ image comparisons. Since in PIV, image correlation is the most time-consuming calculation, a speedup of N_{pairs} is possible with image overlapping. In reality, the low speed of image reading from hard disks prevents image overlapping from achieving this full speedup.

This paper presents a study of the measurement accuracy of the earlier techniques focusing on the novel implementation of image overlapping to reduce measurement depth errors. Both correlation averaging and image overlapping were tested both as standalone techniques and as also in combination with image thresholding and band-pass filtering. The images used in this study were of both simulated and real flows. Figure 5 shows the flow chart of the investigation.

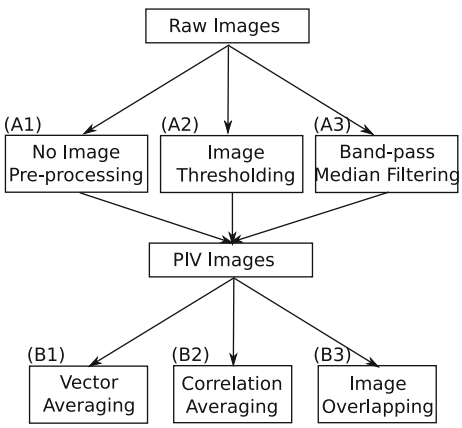

Fig. 5 Image pre-processing and measurement techniques applied to synthetic and experimental images

2 Comparison of performance of image overlapping and correlation averaging using synthetic images

The performance of image overlapping is compared with that of correlation averaging using synthetic data. The main benefit of using synthetic data is that the actual velocity is known allowing validation of the techniques. The comparison was performed on images with and without the use of image pre-processing techniques. The flow studied is the parabolic channel flow shown in Fig. 1, with a channel depth of 200 μm. Specifically, we considered the flow properties at two pertinent locations: the channel center, $z = 0$, and adjacent to the wall, $z = 0.9R$. The second location, $z = 0.9R$, was selected in preference to the actual wall as the theoretical velocity is not zero. As shown in Fig. 2, the measurement accuracy at these locations is significantly affected by the depth of measurement. The optical, particle and flow conditions are the same for all test cases.

2.1 Synthetic image generation

For each measurement location, a total of 2,048 independent image pairs of size 1,024 × 1,024 pixels were generated in 8-bit grayscale. No artificial noise was added into the images, and Brownian motion was not considered. The uniform parabolic displacement profile in z direction generates a maximum displacement of 27.03 pixels between image pairs in the channel center. The velocity in the x and y directions remains constant. Particles of 1 μm diameter are uniformly distributed within the viewing region with particle density of 1.74×10^{-4} particles/μm^3, equivalent to 10,000 particles per image. Particle image formation follows the model employed by Olsen and Adrian [16], with a simulated microscope lens of 10× magnification, 0.30 numerical aperture and 10 mm working distance. The fluorescent wavelength emitted from the particles is 560 nm.

2.2 Image and PIV processings

As shown in Fig. 5, there are three options for pre-processing the raw images: no image pre-processing, image thresholding or band-pass median filtering. Subsequently, there are three ways in which the PIV data can be processed: vector averaging, correlation averaging or image overlapping. A number of cases were investigated to determine the performance of image overlapping relative to existing techniques, with and without pre-processing. The first case follows route A1 to B2/B3, i.e. the velocity was calculated using either correlation averaging or image overlapping directly from the raw images without pre-processing. The second case follows route A2 to B2/B3,

where images pre-processed with image thresholding were processed by either correlation averaging or image overlapping. The third case follows route A3 to B2/B3, where either correlation averaging or image overlapping was applied to images pre-processed by band-pass median filtering. Synthetic images were thresholded using Eq. 3 or band-pass filtered according to Eq. 2 with the first term of the right-hand side being replaced by the image itself.

To study the effect of varying the number of image pairs (N_{pairs}) using in the overlapping and correlation averaging techniques, an image set containing 2,048 pairs was split into 2,048/N_{pairs} image subsets. The measurement techniques were applied to each subset to produce an in-plane velocity field. To make a fair comparison, each result must contain data from the same total number of image pairs, which is 2,048. Vector averaging was applied to velocity measurements from 2,048/N_{pairs} image subsets to provide the final result. When $N_{\text{pairs}} = 1$, the measurement is 100% vector averaging. For PIV processing, each image was divided into non-overlapped regions of 64 × 64 pixels and the velocity calculated within each region. The velocity within each z-plane is the average of these velocities. The standard deviation of the measurements was also obtained for all values of N_{pairs}.

To simplify the data presented in the figures, we define the normalized measured velocity as $U^* = \frac{U_{\text{meas}}(z)}{U_{\text{theory}}(z)}$. In addition, we define the normalized velocity at the center $U_c^* = U_{z=0}^*$, and near the wall as $U_w^* = U_{z=0.9R}^*$.

2.3 Results and Discussion

For the first case studied, the data are processed using correlation averaging and image overlapping with no pre-processing. The effect of increasing N_{pairs} on the measurement accuracy of both PIV techniques is shown in Fig. 6 for measurement locations at the flow center, Fig. 6a, and near wall, Fig. 6b. With increasing N_{pairs} in the center of the channel, Fig. 6a, the measurement using correlation averaging (open triangle) converges rapidly toward $U_c^* = 0.9971$, while this is a good result, correlation averaging is clearly under estimating the velocity. The measurement using image overlapping (empty circle) converges toward the exact value, reaching $U_c^* = 0.9996$. A similar trend is shown in Fig. 6b for the case $z = 0.9R$, except that correlation averaging overestimates the velocity by at least 5%, while image overlapping produces an accurate measurement for sufficiently high N_{pairs} (around 2,048). In addition, with increasing N_{pairs}, the measurement standard deviation of both correlation averaging and image overlapping decreases. As N_{pairs} becomes large, the overlapped images experience particle interference as shown in Fig. 4 and particles lie on top of (or are hidden under) their neighbors. At some point the overlapped image will saturate, thus increasing N_{pairs} does not improve velocity measurement accuracy indefinitely.

In the second test case, the raw data are pre-processed using image thresholding or band-pass filtering. First, we examine the effect of varying threshold level for a fixed number of image pairs (N_{pairs} = 2,048). The velocity measured adjacent to the channel wall, $z = 0.9R$, is shown in Fig. 7 for threshold levels up to 125 where zero threshold level means no image thresholding (corresponding to $N_{\text{pairs}} = 2{,}048$ in Fig. 6b). With increasing threshold level, the near the wall measurement using correlation averaging (filled triangle) converges toward the exact value of $U_w^* = 1$, and the velocity error at threshold value = 75, or 30% of the dynamic range, is only 10% of the error without thresholding. However, as threshold value exceeds 75, the

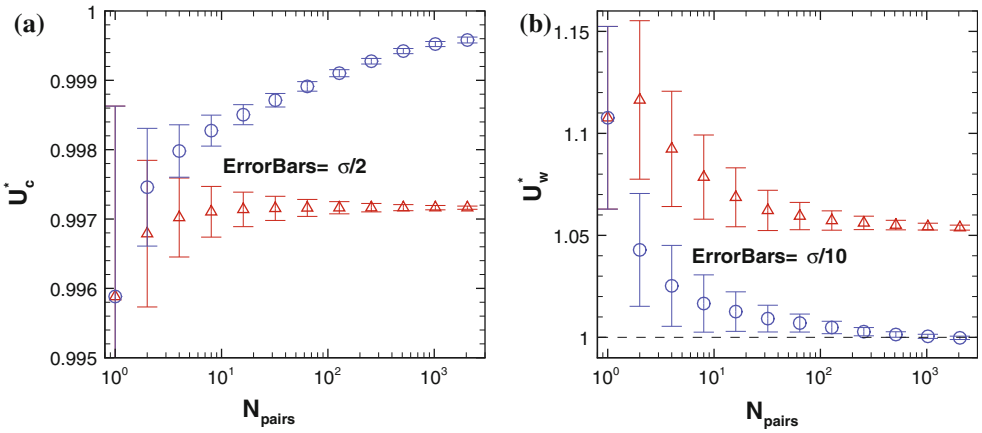

Fig. 6 Correlation averaging versus image overlapping in the flow center, **a** $z = 0$, and near the wall, **b** $z = 0.9R$. The velocity measurements are normalized by the exact velocity at the respective z location. With increasing number of image pairs, both measurements converge toward the true value (1). Image overlapping measurement converges faster and for the same number of image pairs the random error represented by the error bars are smaller than that of correlation averaging. The errorbars plotted are 1/2 and 1/10 of the velocity standard deviation for (**a**) and (**b**), respectively. *Legend*: *open triangle* correlation averaging, *open circle* image overlapping

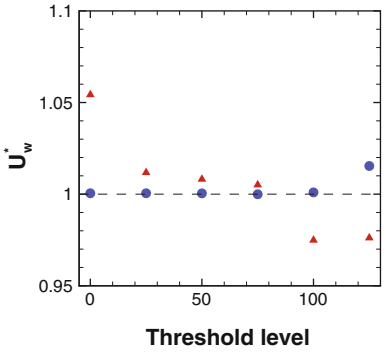

Fig. 7 Effect of image thresholding on correlation averaging and image overlapping velocity measurements near the channel wall. Using the optimum threshold level of 75 in 8-bit grayscale, or 30% of the dynamic range, can significantly improve the measurement accuracy of correlation averaging. Non-dimensional velocity is shown as a function of threshold value for N_{pairs} = 2,048. *Legend*: *filled triangle* correlation averaging, *filled circle* image overlapping

measurement becomes spurious. In contrast, the measurement using image overlapping (filled circle) produces extremely accurate results without image thresholding and is relatively unaffected by increasing threshold values until the threshold reaches 125. The increased error at high threshold values can be explained by the fact that at these values there is little particle information to provide correct velocity measurements. The correlation averaging technique appears to be slightly more sensitive to this "over thresholding" effect. For this data, the optimum threshold level appears to be 75. Clearly, the performance of correlation averaging can be improved by image thresholding, however, in a non-synthetic experiment it is difficult to predict the optimum threshold level.

Additional studies of the effect of varying N_{pairs} on the performance of the optimum threshold show that for sufficient N_{pairs} correlation averaging performs significantly better with thresholding. However, image overlapping is relatively unaffected by image thresholding when $N_{\text{pairs}} > 10$.

Finally for the third test case, an image band-pass filter using a median filter was used prior to the PIV processing. As in the second casem, a fixed number of image pairs, N_{pairs} = 1,024, is used. The effect of band-pass median filtering on the measurements using correlation averaging and image overlapping is shown in Fig. 8 as a function of filter radius. The filter radius is varied from 1 to 32 pixels, i.e. the filter size varies from 3 × 3 pixels to 65 × 65 pixels. The filter radii shown in Fig. 8 are normalized by the diameter of the in-focus particle, D_p = 3.644 pixels. Both Fig. 8a and b show that median filter can improve the measurement accuracy for both correlation averaging and image overlapping, though the improvement in accuracy of the overlapping measurement is minimal. The best measurement accuracy is obtained with smallest filter size of 3 × 3 pixels, or r_{filt}/D_p = 0.274 and the measurement accuracy decreases with increasing r_{filt}/D_p. When $r_{\text{filt}} \geq 32$ pixels, or r_{filt}/D_p = 8.78, the effect of the filter is negligible, and the velocities are approximately equal to the unfiltered data plotted in Fig. 6. In these synthetic images, image overlapping is weakly affected by band-pass median filtering whist correlation averaging is significantly improved. In Sect. 3.2, it will be shown that for experimental images with particle clumping, band-pass median filtering can also significantly improve the performance of image overlapping by removing these clumps.

The comparison of correlation averaging and image overlapping using synthetic images has shown that for all cases considered image overlapping provides better measurement accuracy than correlation averaging. Image preprocessing techniques such as image thresholding and band-pass median filtering can significantly improve the measurement accuracy of correlation averaging; however,

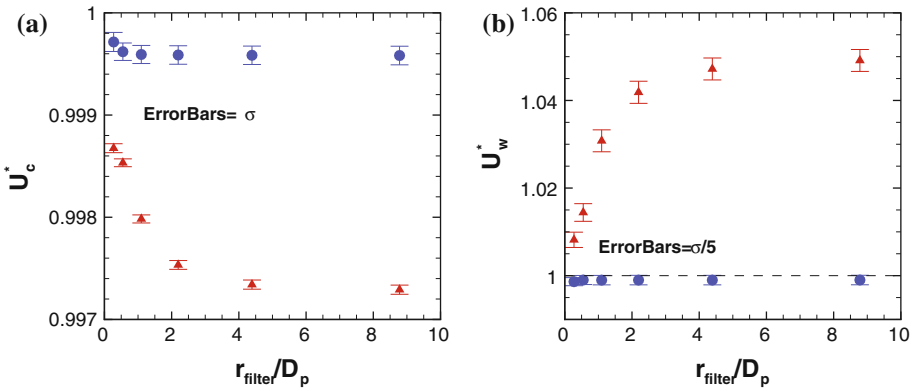

Fig. 8 Effects of band-pass median filtering on correlation averaging and image overlapping measurements as a function of filter radius. **a** At the flow center $z = 0$ and **b** near wall $z = 0.9R$. The number of image pairs used for all cases is 1,024 and for in-focus diameter D_p = 3.644 pixels. For both positions, the smallest error occurs at the smallest filter size. Image overlapping gives the best accuracy and is least sensitive to changes in median filter size. *Legend*: *filled triangle* correlation averaging, *filled circle* image overlapping

its overall measurement accuracy is still inferior than that of image overlapping.

At high N_{pairs}, overlapped images become saturated with particles as shown in Fig. 4d, pixel locking (often referred to as peak locking) can affect the measurement accuracy. Pixel locking is a tendency for measured displacements to consistently "lock" toward integer pixel values (Christensen [8]). To study pixel locking, a new set of synthetic images was generated using similar optical settings, channel size, particle size and seeing density. A total of 2,048 image pairs of 2,048 × 1,024 pixels size were generated at the center plane $z = 0$ of an artificial shear flow. Horizontal displacement between two exposures is $\delta x(y, z) = 0.04y + 0.3z$. Other displacement components were zero. Both correlation averaging and image overlapping were performed on the image set. The histograms of the subpixel parts of the measured displacements (between 0 and 1) are used to study the pixel-locking effect. Figure 9a–b shows the displacement histograms of correlation averaging and image overlapping, respectively. Pixel-locking effect is subtle in both cases, although slightly more visible in correlation averaging than in image overlapping. At N_{pairs} = 2,048, where overlapped images are saturated, the histogram of image overlapping is slightly noisy but does not show any evidence of pixel locking. Trying to increase N_{pairs} much further may increase the uncertainty of the measurement. However, this is unnecessary as there is diminishing improvement when N_{pairs} becomes very large, as shown in Fig. 6a–b. In fact, the maximum N_{pairs} that should be used with image overlapping is sufficiently large that is unlikely to be exceeded for the normal range of number of image pairs acquired during an experiment. When applying image averaging, image saturation can occur, causing significant degradation of measurement accuracy (Meinhart et al. [13]). This problem of image saturation only occurs in cases of extreme numbers of overlapped images when applying the present technique. In brief, the pixel-locking effect in image overlapping is comparable or slightly less than that in correlation averaging, and while image saturation introduces subpixel noise to the measurements of image overlapping it does not result in pixel locking.

3 Performance of image overlapping and correlation averaging on experimental images

This section details the performance of correlation averaging and image overlapping using images obtained from a real experiment conducted in a micro channel. For comparison, the data are processed with or without image preprocessing. Scanning PIV is used to take measurements parallel to the wall throughout the depth of the channel. This allows the extraction of the out-of-plane velocity profile, which can be compared to the theoretical profile. The scanning PIV images were processed using the procedures described in Sect. 2.2 to compare the performance of correlation averaging and image overlapping.

3.1 Method

A schematic the experimental setup is shown in Fig. 10. A syringe pump (Harvard PHD 2000) with a 5 cc syringe perfused glycerol solution through a rectangular channel with a nominal cross-section of 2,000 × 200 μm^2. The constant flow rate of 0.02 ml/min results in a maximum velocity of 1.364 mm/s at the channel center corresponding to a maximum displacement of 19.5 pixels in the recorded images. The glycerol solution was made from a mixture of 2 ml glycerin, 8 ml water and 1 ml fluorescent particle

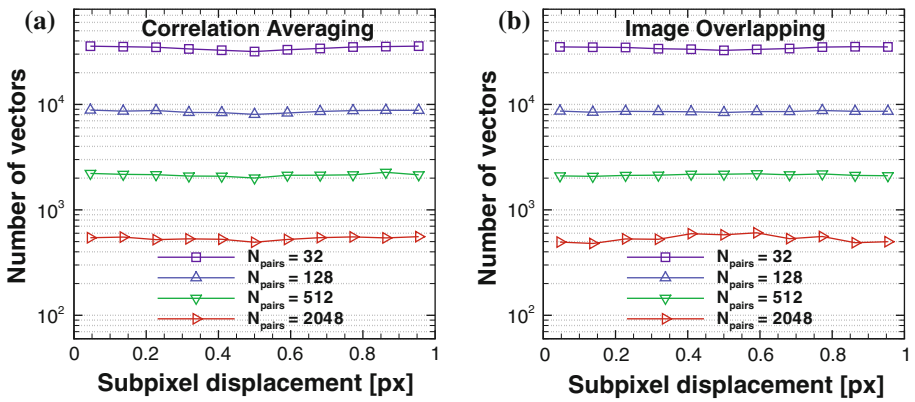

Fig. 9 Pixel-locking effect based on the histograms of subpixel displacements by **a** correlation averaging and **b** image overlapping for various values of image pairs N_{pairs}. At N_{pairs} = 32, pixel locking is visible in both correlation averaging and image overlapping. With increasing N_{pairs}, pixel locking decreases. For N_{pairs} = 32, 128 and 512, image overlapping has less pixel- locking effect that correlation averaging. At N_{pairs} = 2,048, where overlapped images are saturated with particles, the histogram of image overlapping measurement is noisy but no obvious pixel locking is found

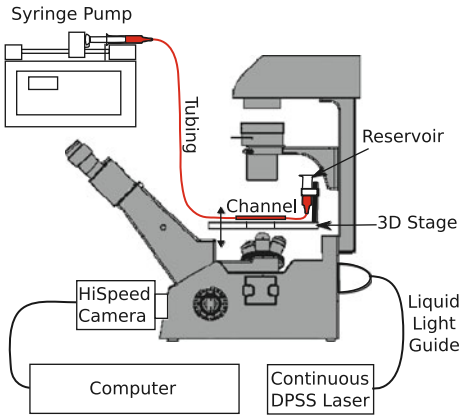

Fig. 10 Experimental setup for micro PIV. Glycerol solution is perfused through the micro channel into a reservoir. The channel is scanned in vertical direction by a computer-controlled 3D stage. A continuous laser beam passes though the liquid light guide to illuminate the channel. The particles in the channel are imaged through the microscope by a high-speed camera

suspension (1% solid). The glycerol solution had density 1.05 g/cm^3 and viscosity 1.76 *cP*. The Reynolds number based on mean velocity and channel height is $Re_{U\_\mathrm{mean}} = 0.11$ and, therefore, the flow can be considered as a Poiseuille flow. The fluorescent particles, 3 μm diameter with a relative density of 1.05, had an emission wavelength of 612 nm. The average particle seeding density in the glycerol solution was 6.43×10^{-5} particles/μm^3. However, the seeding density was observed to decrease near the channel walls.

The refractive index of the glycerol solution causes the 200 μm high channel to have an apparent height of 147.06 μm when viewed with the objective through air. The channel was displaced relative to the microscope objective using a computer-controlled 3D stage with submicron accuracy. A stage scanning step of 2.5 μm was used, corresponding to a 3.4 μm displacement of the focal plane inside the glycerol filled channel, and 59 steps were required to transverse the channel height.

Images were captured in the center of the channel width, using a 10× objective lens with $NA = 0.30$ and a working distance of 10 mm. Volume illumination was provided by a continuous diode pumped solid state laser (Melles Griot) emitting at 532 nm and transmitted to the microscope through a liquid light guide (Leica). A MotionPro X5 intensified camera (IDT) captured 1024 image pairs, 512 × 512 pixels in size, at each of 65 scanning locations throughout the channel height. To implement the overlapping technique, the time between image pairs was selected such that in the slowest regions the particles move more than one particle diameter between image pairs.

PIV correlation used templates of 128 × 128 pixels to calculate the velocity for all measurements techniques. Vector averaging, correlation averaging and image overlapping without/with image pre-processing (as shown in Fig. 5) were performed to compare their measurement accuracy. Velocity measurements are reported in terms of pixel displacements δx.

The measured velocity profiles were then compared with a theoretical pressure-driven Poiseuille profile in a rectangular channel, White [24]. For quantitative comparison between the velocity measurements and the theoretical profile, the norm of the difference was calculated for each measurement technique, where the norm, l^2_{norm}, is defined as:

$$l^2_{\mathrm{norm}} = \sqrt{\sum_{z=-R}^{R} \left(U_{\mathrm{theory}}(z) - U_{\mathrm{meas}}(z)\right)^2} \tag{8}$$

3.2 Experimental results and discussion

The experimental images present a number of challenges, which are not present in the synthetic data. Unlike the synthetic images, the experimental images contain significant noise from various sources including high-frequency noise due to low-light conditions and sensor dark current. The particles are of non-uniform diameter; and therefore, their brightness is non-uniform. Also in these experiments, particles occasionally adhere to each other forming large and bright particle clumps and skewing the velocity measurement toward the velocity of the clumps. The effect of these clumps is greatest on the overlapping technique, as will be discussed later. In addition, due to particle interaction with the wall, the concentration of the seeding particles is significantly lower close to the walls (Moger et al. [14], Cao and Wereley [7], and Li and Yoda [11]). The reduction in seeding density near the walls will also skew velocity measurements toward the higher-velocity particles in the regions of higher concentration further from the wall.

The velocity profile obtained by vector averaging with no pre-processing in Fig. 11a is the baseline case. The measured velocity is compared with the theoretical Poiseuille flow showing, as expected that the measurements underestimate the velocity in the channel center and overestimate it near wall. The standard deviation of the measurements, represented by the error bars, is significant across the flow. The value of l^2_{norm} is a relative measure of the performance compared to the theoretical values averaged over the channel depth.

The velocities measured by correlation averaging alone, Fig. 11b, are very similar to those measured with vector averaging as indicated by the similar l^2_{norm} value. However, the standard deviation of the correlation averaging measurements is significantly smaller. The performance of correlation averaging can be improved by image preprocessing as illustrated in Fig. 11c and d, with the application of optimum image thresholding and image band-pass

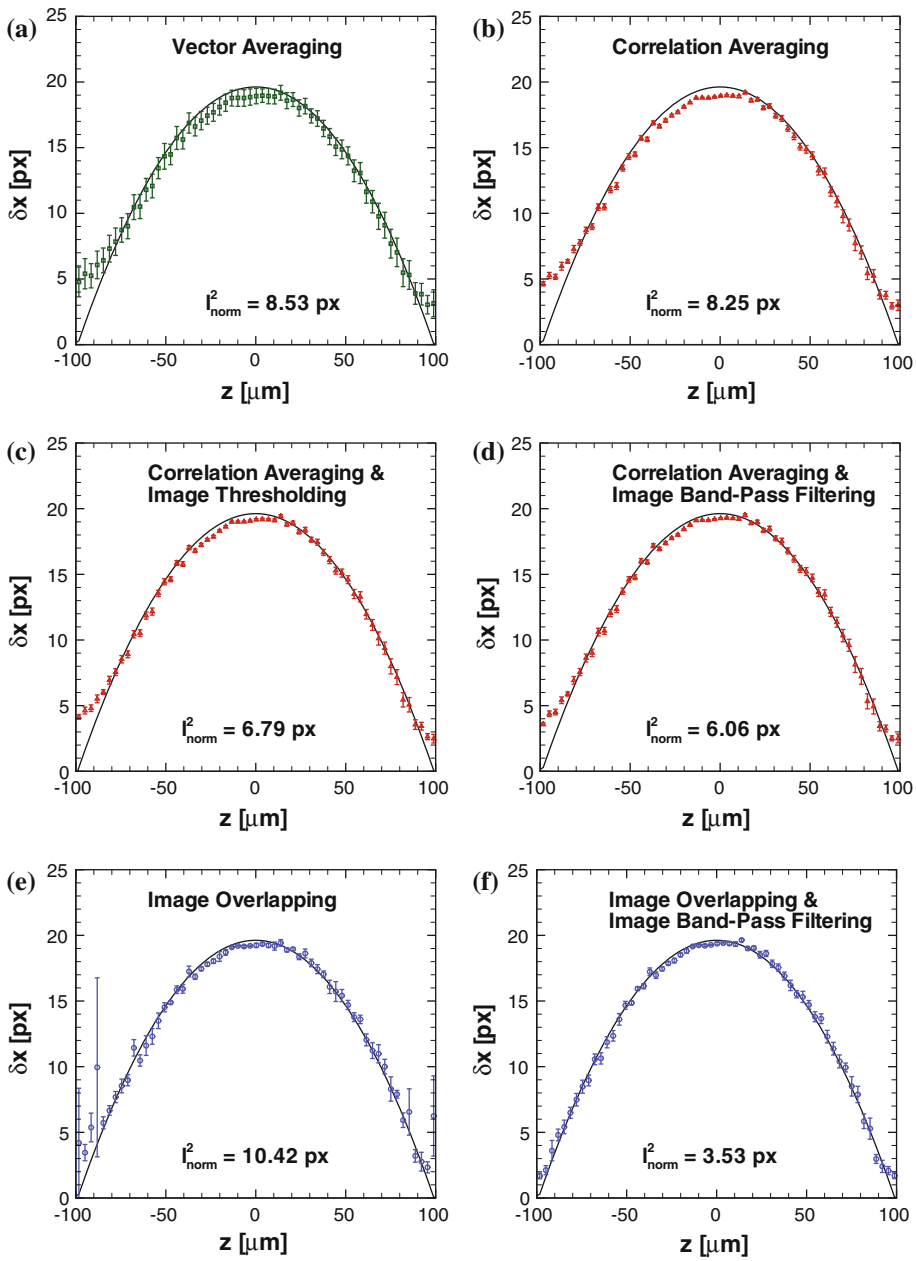

Fig. 11 Measured velocity profiles of experimental channel flow obtained with different image processing techniques, error bars represent the standard deviation and solid curves the theoretical Poiseuille velocity profile. I^2_{norm} decreases from 8.53 *px* with **a** vector averaging only, to 8.25*px* with **b** correlation averaging only, to 6.79 *px* with **c** correlation averaging & image thresholding (threshold value = 25, or 10% of the image dynamic range), to 6.06 *px* with **d** correlation averaging & image band-pass filtering (r_{filt} = 7 *px*), to 3.53 *px* with **f** image overlapping & image band-pass filtering (r_{filt} = 7 *px*). **e** Image overlapping alone suffers large errors due to particle clumps, which are removed by band-pass filtering. A reduction of 57% in I^2_{norm} is achieved using image overlapping with image pre-processing instead of standard correlation averaging, with the greatest improvement in velocity measurements occurring near the wall

filtering, respectively. The optimum threshold level was 25 in 8-bit grayscale, or 10% of the image dynamic range, lower than the level 30% found using synthetic images possibly due to lower particle intensity in experimental image and background noise. The improvements were most significant in the flow center and near the wall. A considerable decrease in I^2_{norm} was obtained.

Image overlapping without pre-processing can be adversely affected by the presence of particle clumps as demonstrated by the poor performance of image overlapping in Fig. 11e. The bright particle clumps are preferentially collected in the overlapped image even when they are far from the measurement plane as shown in Fig. 12a. This figure clearly shows three particle clumps each of which appears at least three times as the flow moves from left to right. Clearly, the velocity of the biggest clump, approximately 1/3 down the image, is higher than the velocity of the clumps above and below it. The resulting velocity measurement at $z = -88$ μm in Fig. 11e is clearly erroneous. However, by applying band-pass filtering with r_{filt} = 7 pixels, most particles clumps are removed from the overlapped images, as shown in Fig. 12b, producing the excellent velocity measurements as shown in Fig. 11f. The I^2_{norm} value of obtained when image band-pass filtering is applied to image overlapping (I^2_{norm} = 3.53) is almost half that of correlation averaging with optimum image

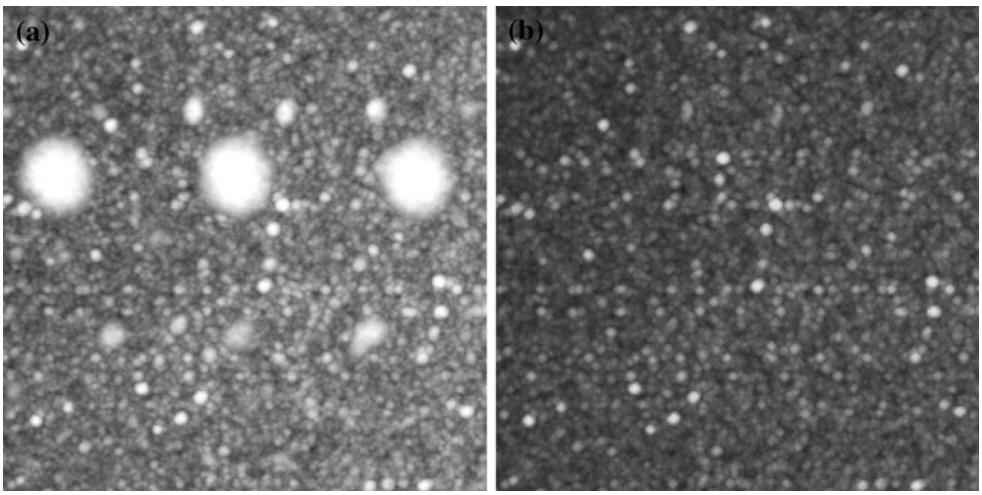

Fig. 12 Overlapped images with N_{pairs} = 1,024 used to calculate the velocity data point at $z = -88$ μm in Fig. 11e and f (cropped to 256 × 256 pixels). **a** The original overlapped image without band-pass median filtering containing three large particle clumps, each of which appears three times in the overlapped image. Clearly, these clumps are not moving at the same velocity consistent with the large error in the 4th data point from the left of Fig. 11e. **b** The overlapped image after band-pass median filtering has removed the largest clumps and causing the smaller clumps to become weaker. This reduces the measurement error as shown in Fig. 11f

pre-processing (l^2_{norm} = 6.06). In particular, the accuracy is significantly improved in the near wall region where the velocity gradients are greatest. The application of image thresholding to the overlapping technique (not shown) does not remove the particle clumps and produces little improvement in accuracy. This result shows that even in images with particle clumps with appropriate pre-processing, image overlapping can produce a significantly better measurement accuracy than correlation averaging.

There is a slight asymmetry in the measured velocity profiles of Fig. 11a–d. This can be explained by the fact that although the particle density is approximately equal to the flow solution, it was observed that particles with lower density concentrate near or even occasionally adhered to the channel upper wall ($z = +100$ μm), while the particle concentration at the lower wall ($z = -100$ μm) is lower. Measurements using vector and correlation averaging (Fig. 11a–d) have a relatively large depth of measurement, and the velocities measured near the walls are biased by the higher velocity flow toward the center of the channel. This affect is magnified on the lower wall ($z = -100$ μm) as the number of particles actually at the measurement plane is lower, resulting in a non-symmetric velocity profile. Similarly, the particle clumps contaminating image overlapping without image pre-processing (Fig. 12a) have a greater effect when the seeding density at the measurement plane is lower, causing more significant error in the left-hand side of Fig. 11e. Once the particle clumps are removed (Fig. 12b), the reduced depth of measurement of the overlapping technique produces a velocity profile, which is much more symmetrical (Fig. 11f).

4 Conclusion

The velocities measured using micro PIV are biased by the velocities of out-of-focus particles within a thickness defined by the depth of correlation. The application of image overlapping to reduce the depth of measurement can significantly reduce these errors. This was illustrated using channel flow where compared to standard correlation averaging, image overlapping produced a 57% reduction in the value of l^2_{norm}. The improvements in measurement accuracy were greatest in the near wall regions.

Image overlapping is performed by taking maximal intensities from an image set to produce a single overlapped image. PIV correlation is applied only once on an pair of overlapped images to produce an average velocity measurement. As the in-focus particles are brightest, they are accumulated in the overlapped image. As a result, the measurement using an overlapped image pair provides the velocity of particles close to the focal plane. This effectively reduces the depth of measurement and the associated errors. An additional advantage of image overlapping is that only a single correlation is performed making it significantly faster than correlation averaging. The accuracy of image overlapping improves as more images are overlapped until for a large number of images the overlapped image begins to saturate with particles. Experimental images containing clumps of particles may require image pre-processing to remove these clumps before image overlapping can be effective.

Correlation averaging has for the past decade been the gold standard in micro PIV processing. However, using both synthetic and experimental images, image overlapping

was shown to out-perform correlation averaging, particularly in regions which suffer, significant bias effects due to out-of-focus particles. For synthetic images without particle clumps, image overlapping out-performs correlation averaging even when correlation averaging is optimized using image pre-processing. Fully optimized image thresholding and band-pass filtering significantly improve the measurement accuracy of correlation averaging; however, the optimum settings are difficult to predict without knowing the exact velocity beforehand. In contrast, image overlapping always produces optimum results and is only weakly affected by image pre-processings. For experimental images containing particle clumps, the measurements using image overlapping without pre-processing suffer bias errors from the clumps. With the application of band-pass filtering to remove the clumps, image overlapping continues to produce the best measurement accuracy. Image overlapping with band-pass filtering reduces by 57% the measurement errors compared to that of plain correlation averaging and reduces by 42% the measurement errors compared to that of correlation averaging with band-pass filtering.

Image overlapping was found to have comparable or slightly reduced pixel-locking effects compared to correlation averaging. Image overlapping with very large number of image pairs resulted in image saturation, reduced incremental improvement of accuracy, and increased measurement subpixel noise, but no visible peak locking was found.

In summary, image overlapping produces significantly improved measurement accuracy with significantly less computational effort than correlation averaging. This simple algorithm reduces the depth of measurement, producing significant improvement in the accuracy of velocity measurements in regions where the measurements would otherwise be biased by the velocities of out-of-focus particles. Image overlapping presents an opportunity to easily improve measurement accuracy in the critical wall region and thus is particularly relevant to biological flows.

References

1. Adrian RJ (1988) Double exposure, multiple-field particle image velocimetry for turbulent probability density. Optics Lasers Eng 9:211–228
2. Adrian RJ (2005) Twenty years of particle image velocimetry. Exp Fluids 39:159–169
3. Bitsch L, Olesen L, Westergaard C, Bruus H, Klank H, Kutter J (2005) Micro particle-image velocimetry of bead suspensions and blood flows. Exp Fluids 39:507–513
4. Bourdon CJ, Olsen MG, Gorby AD (2004) Power-filter technique for modifying depth of correlation in microPIV experiments. Exp Fluids 37(2):263–271
5. Bourdon C, Olsen M, Gorby A (2004) Validation of an analytical solution for depth of correlation in microscopic particle image velocimetry. Meas Sci Technol 15:318–327
6. Bourdon CJ, Olsen MG, Gorby AD (2006) The depth of correlation in micro-PIV for high numerical aperture and immersion objectives. J Fluids Eng 128:883–886
7. Cao J, Wereley ST (2006) Micro-particle image velocimetry in biomedical applications. In: Bowlin GL, Wnek G (eds) Encyclopedia of biomaterials and biomedical engineering, 2nd edn. Informa Healthcare, New York, pp 1873–1884
8. Christensen KT (2004) The influence of peak-locking errors on turbulence statistics computed from PIV ensembles. Exp Fluids 36:484–497
9. Gui L, Wereley ST, Lee SY (2002) Digital filters for reducing background noise in micro PIV measurement. In 11th international symposium on the application of laser techniques to fluid mechanics, Lisbon
10. Kiger KT, Pan C (2000) PIV Technique for the simultaneous measurement of dilute two-phase flows. J Fluids Eng 122:811–818
11. Li H, Yoda M (2008) Multilayer nano-particle image velocimetry (MnPIV) in microscale Poiseuille flows. Meas Sci Technol 19:075402
12. Lindken R, Westerweel J, Wieneke B (2006) Stereoscopic micro particle image velocimetry. Exp Fluids, Springer 41:161–171
13. Meinhart CD, Wereley ST, Santiago JG (2000) A PIV Algorithm for estimating time-averaged velocity fields. J Fluids Eng 122:285–289
14. Moger J, Matcher SJ, Winlove CP, Shore A (2004) Measuring red blood cell flow dynamics in a glass capillary using Doppler optical coherence tomography and Doppler amplitude optical coherence tomography. J Biomed Optics 9:982–994
15 Nesbitt W, Westein E, Tovar-Lopez F, Tolouei E, Mitchell A, Fu J, Carberry J, Fouras A, Jackson SA (2009) Shear gradient-dependent platelet aggregation mechanism drives thrombus formation. Nat Med 15:665–673
16. Olsen MG, Adrian RJ (2000) Out-of-focus effects on particle image visibility and correlation in microscopic particle image velocimetry. Exp Fluids 29(7):S166–S174
17. Olsen MG, Adrian RJ (2000b) Brownian motion and correlation in particle image velocimetry. Optics Laser Technol 32:621–627
18. Olsen MG, Bourdon CJ (2003) Out-of-plane motion effects in microscopic particle image velocimetry. J Fluids Eng 125:895–901
19. Olsen MG (2009) Directional dependence of depth of correlation due to in-plane fluid shear in microscopic particle image velocimetry. Meas Sci Technol 20:015402 (9 pp)
20. Perreult S, Herbert P (2007) Median filtering in constant time. IEEE transactions on image processing 16:2389–2394
21. Santiago J, Wereley S, Meinhart C, Beebe D, Adrian R (1998) A particle image velocimetry system for microfluidics. Exp Fluids 25:316–319
22. Wereley ST, Gui L, Meinhart CD (2002) Advanced algorithms for microscale particle image velocimetry. AIAA J 40:1047–1055
23. Wereley ST, Meinhart CD, Gray MHB (1999) Depth effects in volume illuminated particle image velocimetry. In Third international workshop on particle image velocimetry, Santa Barbara, CA, USA
24. White FM (1991) Viscous fluid flow, 2nd edn. McGraw-Hill Book Company, Singapore, pp 114–121
25. Zheng X, SilberLi Z (2008) Measurement of velocity profiles in a rectangular microchannel with aspect ratio $\alpha = 0.35$. Exp Fluids 44:951–959